Electronic Supplementary information (ESI)

Enhanced Ferroelectric Photovoltaic Effect in Semiconducting Single-Wall Carbon Nanotubes/$BiFeO_3$ Heterostructure Enabled by Wide-Range Light Absorption and Efficient Charge Separation

Hojin Lee[a,b], Hyo-Sun Kim[a,b], Oh Yeong Gong[c], Jun Young Kim[c], Jin Hong Kim[d], Jin Sik Choi[d], Hyun Suk Jung[c], Jun-Young Park[b], Dong Hoe Kim[b], Young-Soo Seo[a,b]*, and Taekjib Choi[a,b]*

a) Hybrid Materials Research Center, Sejong University, Seoul 05006, Korea

b) Department of Nanotechnology and Advanced Materials Engineering, Sejong University, Seoul 05006, Korea

c) School of Advanced Materials Science & Engineering, Sungkyunkwan University, Suwon 16419, Korea

d) Department of Physics, Konkuk University, Seoul 05029, Korea

Corresponding author: ysseo@sejong.ac.kr; tjchoi@sejong.ac.kr

Table S1. Comparison of photovoltaic studies in ferroelectric $BiFeO_3$ (BFO) materials. $SrRuO_3$ (SRO); Al_2O_3-ZnO (AZO); Indium tin oxide (ITO); $La_{0.67}Sr_{0.33}CoO_3$ (LSCO); Fluorine doped Tin Oxide (FTO) coated glass; External quantum efficiency (EQE)

Device Structure	V_{oc} (V)	J_{sc} (mA cm^{-2})	Light intensity (mW cm^{-2})	Efficency (%)
ITO/BFO/SRO[1]	0.8	1.5	285	10 (EQE)
AZO/BFO/FTO[2]	0.63	0.13	100	7 (EQE)
AZO/BFO/LSCO[3]	0.22	0.004	1	-
Pt/BFO/Pt[4]	20	0.05	100	0.00003
Pt/BFO/SRO[5]	0.08	0.063	100	-
Nb:STO/BFO/Au[6]	0.04	6	285	0.03
ITO/BFO/Pt[7]	16	0.12	285	0.125
Graphene/BFO/Pt[8]	0.55	0.025	100	-

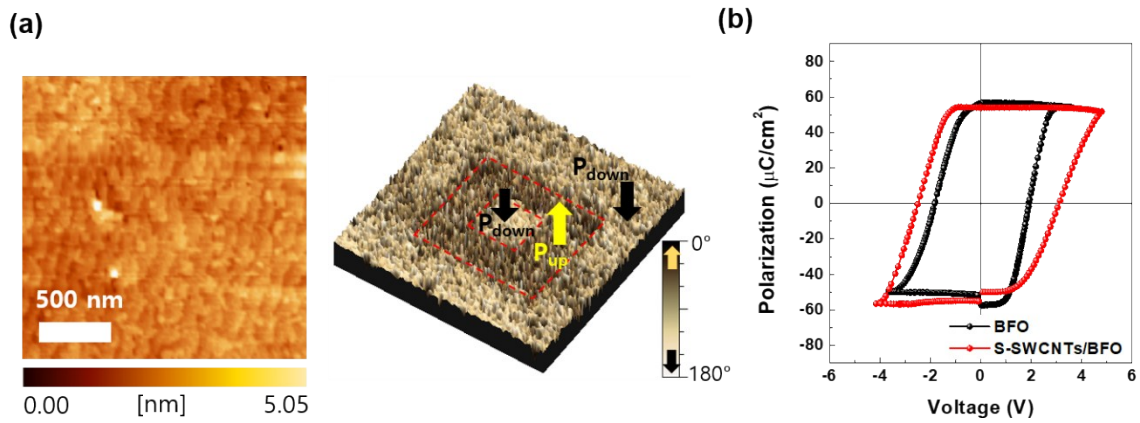

Fig. S1. (a) AFM topographic image (left panel) and PFM phase image (right panel) of BFO/Nb:STO. (b) Polarization-Voltage (*P-V*) hysteresis loops of BFO (black) and S-SWCNTs/BFO (red), respectively, obtained by using the PUND method at 2 kHz.

The surface of BFO thin film (~40 nm) grown on surface-treated Nb:STO is atomically flat with a typical root-mean-square roughness below 0.4 nm. A 3-dimensional out-of-plane piezoresponse phase image (5×5 μm^2) after poling (±5 V), showing clear evidence of ferroelectricity. The white contrasts correspond to the 'downward' polarization state, while the dark ones represent the polarization 'upward' state. We also confirmed the ferroelectricity of samples by measuring *P-V* hysteresis loops, obtained from typical positive-up-negative-down (PUND) method.[9] **Fig. S1b** shows the fully saturated *P-V* loops for BFO and S-SWCNTs/BFO structures. The measured remnant polarization values are almost the same as ~ 55 $\mu C/cm^2$. The coercive voltages of S-SWCNTs/BFO are higher than those of BFO, caused by an additional voltage drop on the S-SWCNTs layer.

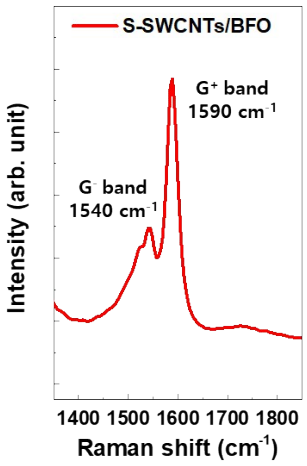

Fig. S2. Raman spectra of S-SWCNTs/BFO heterostructure in a range of G band.

The G bands in the Raman spectra of SWCNTs show a doublet structure that usually spits into G^+ and G^- components. The line profile and the intensities of G^+ and G^- peaks can determine the diameter and chiral indices of SWCNTs.[10] The G^+ band is related to valence vibrations of armchair nanotubes perpendicular to nanotube axis and the G^- band corresponds to valence vibrations of zigzag nanotubes parallel to the nanotube axis. The shape of the G^- component is highly sensitive to whether the SWCNTs are metallic (a broad structure) or semiconducting (single-component G^- band with relatively low intensity).

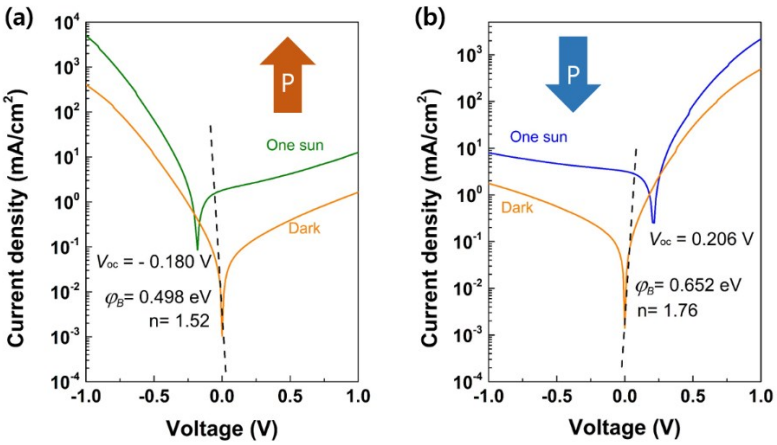

Fig. S3. Semi-log *J-V* curves for (a) Positive-forward (P_{up}) and (b) Negative-forward (P_{down}) diodes in Pt/BFO/Nb:STO structure.

Effective barrier height was estimated by using equations,

$$I = I_0\left[\exp\left(\frac{eV}{nk_BT}\right) - 1\right]$$

$$I_0 = \frac{4\pi em^* k_B^2}{h^3} ST^2 exp(-\frac{\varphi_B}{k_BT})$$

where e is electron charge, *n* an ideality factor, k_B Boltzmann's constant, S the area of electrode, T the temperature, φ_B the Schottky barrier heights, m* the effective mass, *h* Planck constant, and I_0 the saturation current.

The effective interface barrier heights of positive-forward (P_{down}) and negative-forward (P_{up}) diodes can be estimated as 0.652 eV (Pt/BFO) and 0.498 eV (BFO/Nb:STO), respectively. The difference in the effective interface barrier heights may yield asymmetric diode-like behavior and the resultant photovoltaic responses with polarization switching.

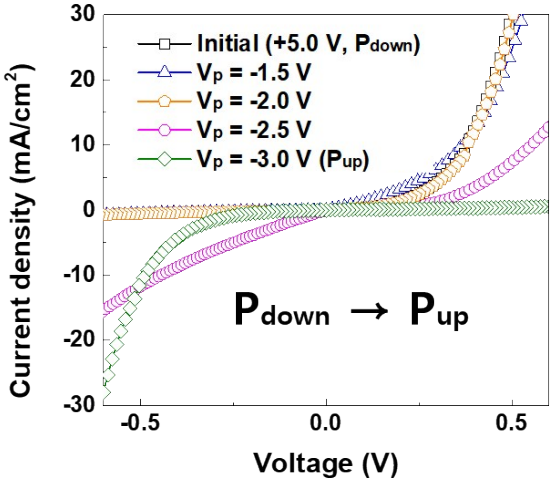

Fig. S4. *J-V* curves for Pt/BFO/Nb:STO, measured after applying opposite-polarity pulse with an incrementally increasing pulse amplitude (V_p).

Initially, by applying voltage pulse of 5 V for 10 ms, we obtained a positive-forward diode behavior with P_{down} state, and then we applied an opposite-polarity pulse (V_p) for 10 ms. Note that we measured *J-V* curves by sweeping voltage of ±1 V below coercive voltages after applying each negative-polarity pulse voltages.

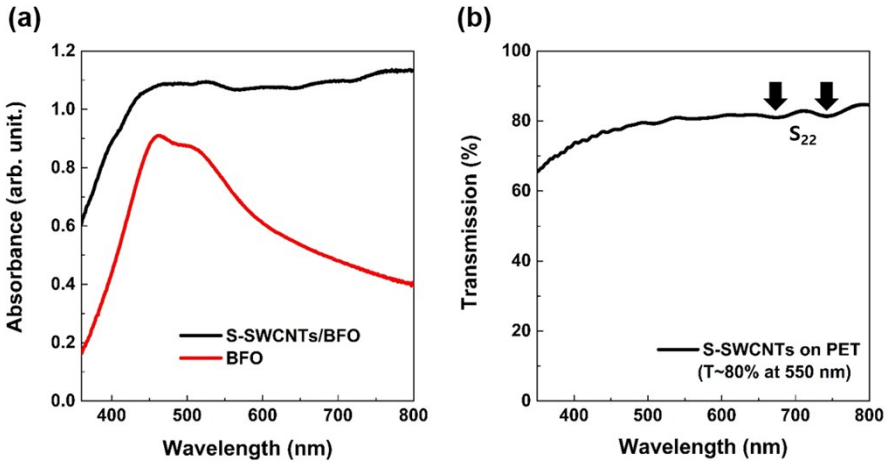

Fig. S5. (a) UV-vis absorption spectra of BFO and S-SWCNTs/BFO heterostructure. (b) Optical transmission spectrum of S-SWCNTs film on PET substrate with 80 % transparency at λ= 550 nm.

The room-temperature optical absorption spectra in the range of 350 nm to 800 nm for BFO and S-SWCNTs/BFO are shown in **Fig. S5**. It is calculated by reflection mode to get rid of component of Nb:STO. BFO (red line) shows the strong spectra in the 450-560 nm range, which are ascribed to the bandgap (2.2-2.7 eV) absorption. S-SWCNTs/BFO (black line) exhibits an apparent enhancement of absorption throughout the wide-range from visible to infrared region due to relatively lower bandgap of S-SWCNTs. In addition, the transmission spectra of S-SWCNTs film deposited on PET substrate were recorded in UV-Vis-NIR range (from 350 nm to 800 nm). The transparency of the S-SWCNTs film at 550 nm was 80 %, while the transparency slightly decreased to ~65% below 500 nm. Moreover, it is evident from the optical transmission spectrum that the majority of S-SWCNTs film has S_{22} bands. Generally, the optical absorption of S-SWCNTs is determined by chirality. Our S-SWCNTs film exhibits the characteristic peaks at 680 nm (1.82 eV) and 730 nm (1.69 eV), respectively, which is in good agreement with S_{22} bands in the literature.[11] The S-SWCNTs film was observed to have a rough surface with relatively high porosity, thus we believe that the light can pass through the S-SWCNTs layer and reach the S-SWCNTs/BFO heterojunction with less interference.

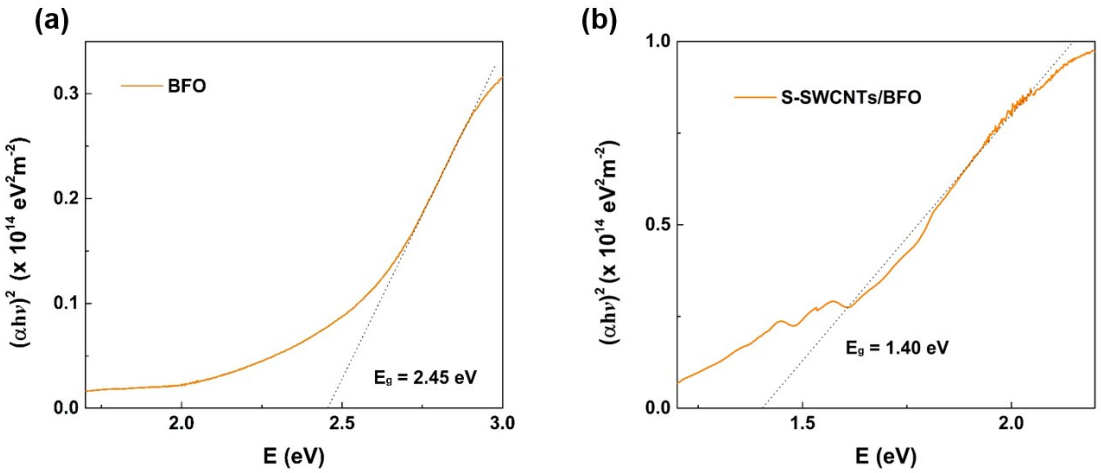

Fig. S6. Tauc's plot for extraction of the optical bandgap of (a) BFO and (b) S-SWCNTs/BFO.

The optical band gap can be determined by extrapolating the linear region of the curves to the energy axis. The optical band gap for BFO and S-SWCTs/BFO from Tauc plot were 2.45 eV and 1.40 eV, respectively.

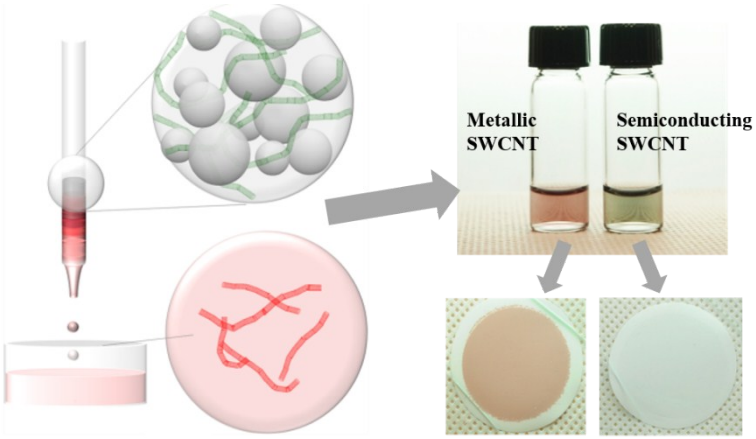

Fig. S7. Schematic representation of the agarose gel chromatography method to separate metallic and semiconducting-SWCNTs. These SWCNTs were classified into M-SWCNTs (reddish solution), S-SWCNTs (greenish solution) by analyzing optical properties according to elution order.

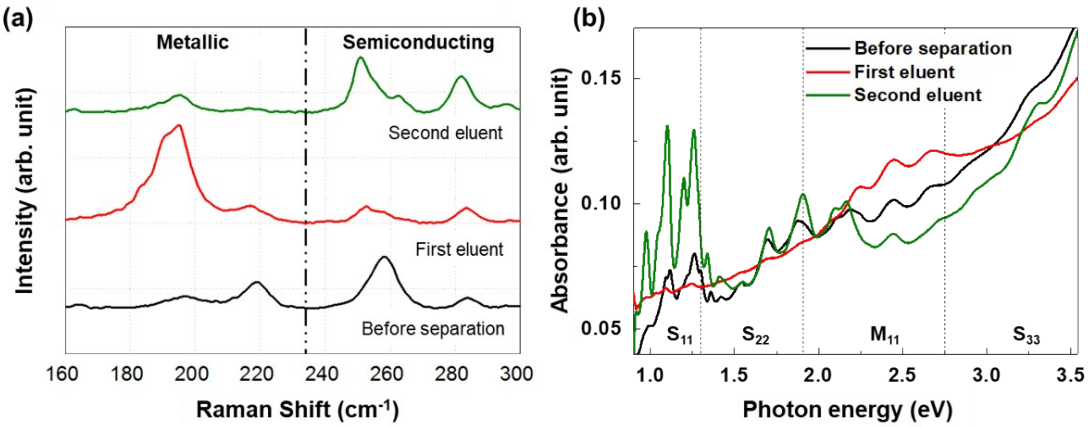

Fig. S8. (a) Radial breathing mode Raman spectra of SWCNTs eluent excited by 633 nm laser. The dashed line separates the metallic and the semiconducting SWCNTs regions. (b) Light absorption spectra at normal incidence of SWCNTs eluents.

The spectrum for the pristine SWCNTs (before separation) was measured as a reference. The region is divided into S_{11}, S_{22}, M_{11}, and S_{33}, in different light absorption area by chirality depending on the structure.[11] The absorption of S-SWCNTs in a range of 950–1350, 650–950, and 300–450 nm seems to enable a wide range absorption in our heterostructures.

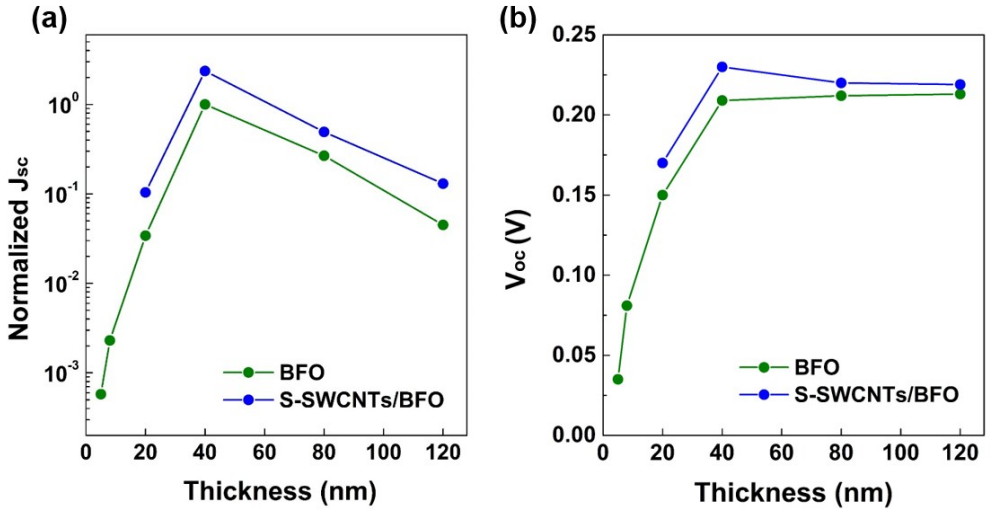

Fig. S9. The comparison of (a) normalized short-circuit photocurrent density (J_{sc}) and (b) open-circuit photovoltage (V_{oc}) for pristine BFO and S-SWCNTs/BFO devices as a function of BFO thickness in P_{down} state under one sun illumination.

The S-SWCNTs/BFO and BFO photovoltaic devices with optimum performance can be obtained by optimizing the film thickness. As can be seen in **Fig. S9**, we compared J_{sc} and V_{oc} of pristine BFO and S-SWCNTs/BFO devices as a function of thickness of ferroelectric BFO in the P_{down} state under one sun illumination. J_{sc} increases monotonically as the thickness decreases from 120 nm to 40 nm due to reducing resistance, while as the thickness further decreases to 20 nm, 8 nm, and 5 nm, the photocurrent rapidly decreases due to high leakage currents (resulting from tunneling) and lower solar absorption (higher transmittance) of BFO.

According to the ferroelectric photovoltaic physics, in case of bulk photovoltaic effect and depolarization effect as photovoltaic mechanisms[12-15], the V_{oc} would increase with thickness of ferroelectric materials. In contrary, BFO and S-SWCNTs/BFO devices showed the weak dependence of V_{oc} on thickness from 120 nm to 40 nm. However, at such small thickness below 40 nm, the shunt resistance due to leakage current becomes lower, which would deteriorate V_{oc}.

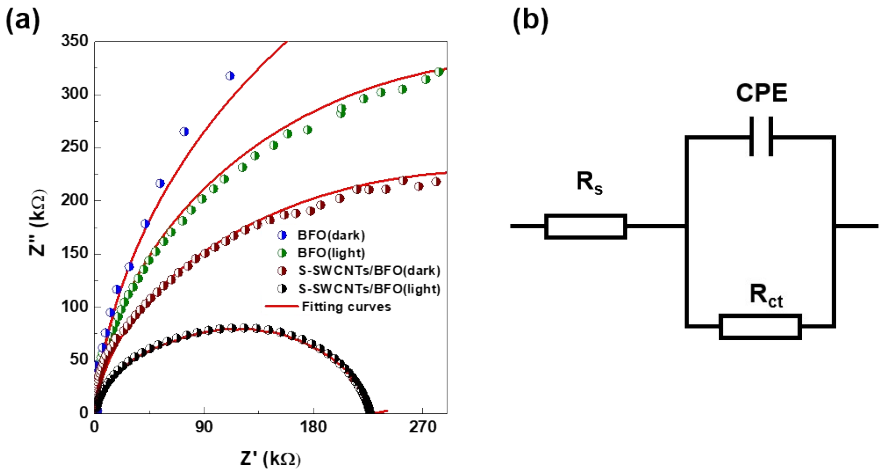

Fig. S10. (a) Electrochemistry impedance spectroscopy of BFO and S-SWCNTs/BFO characterized at V_{oc} in the dark and under illumination, respectively. (b) The equivalent circuit model to fit the spectra.

Electrochemistry impedance spectroscopy (EIS) has been performed to elucidate the charge transfer and transport processes in solar cell.[16, 17] Equivalent circuit (composed of series and/or parallel combination of resistors and capacitors) models have been commonly used to fit and interpret EIS data, where a series resistance R_s connects with a parallel combination of a charge transfer resistance R_{ct} and the capacitance C. Note that R_s remains at the high frequency intercept. As the frequency decreases the capacitive impedance increases, and the capacitive impedance would be infinitely large but the R_{ct} is still remains. As shown in Fig. S6, according to simplified Randle's circuit the plot has a semicircle, in which the maximum of the Z" occurs at $Z' = R_s+R_{ct}/2$, corresponding to the characteristic frequency of the charge transfer processes. Thus, comparison of the semicircles for BFO and S-SWCNTs/BFO clearly demonstrates that the smaller semicircle of S-SWNCTs/BFO is attributed to the smaller charge transfer resistance.

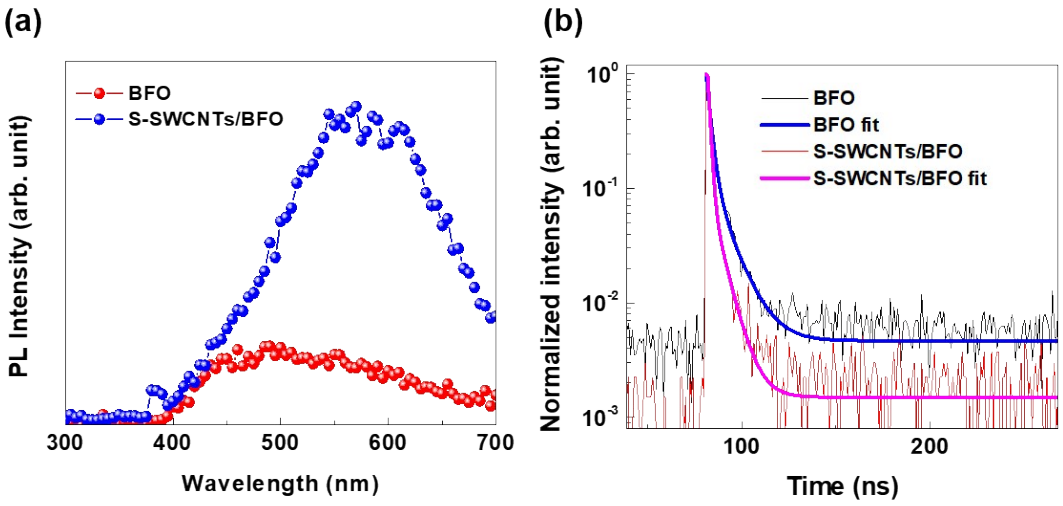

Fig. S11. (a) Steady-state photoluminescence spectra and normalized time-resolved photoluminescence spectra of BFO and S-SWCNTs/BFO with fit lines by Bi-exponential function.

Photoluminescence (PL) measurement has been performed to understand the carrier transfer and recombination of the devices. Steady-state PL is useful in determining the excitation wavelength for the emission spectrum. Shift of PL peaks represent the radiative recombination in band-to-band transition. The BFO thin film has a band with a maximum at 490 nm, while the band of S-SWCNTs is shifted to a long wavelength region (570 nm). The quenching of PL decay, displaying a reduction in the PL signal is associated with the surface recombination at the interface.[18, 19] In other words, the PL signal quenching results from the efficient carrier transfer to the interface which may involve carrier extraction from the active absorber to carrier transport layers and possible recombination due to interfacial defects.

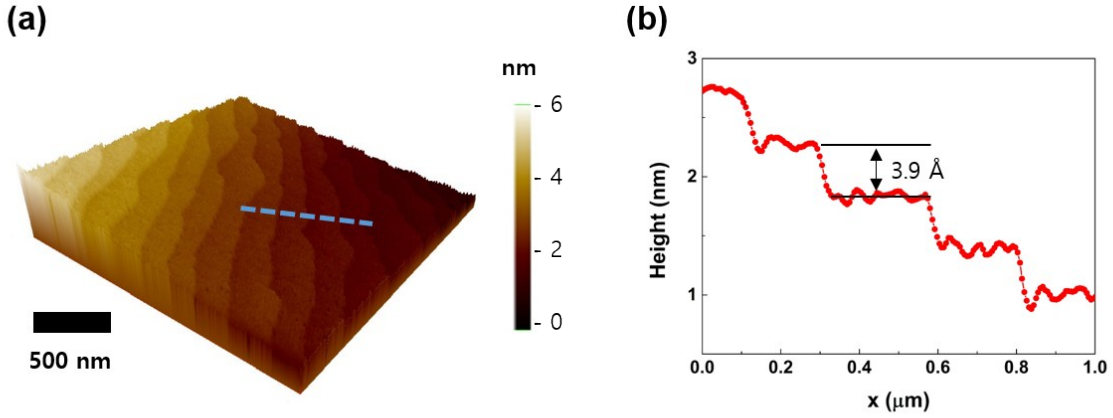

Fig. S12. (a) A three-dimensional AFM image of a chemically and thermally prepared Nb:STO (001) surface. (b) A line profile across the image, indicating atomically flat surface with one unit-cell step height.

For producing atomically flat and chemically single terminated surface of Nn:STO single crystal, we carried out chemical etching and thermal annealing for Nb:STO single crystal. The typical procedures of the wet acidic surface treatment: (1) To removes contaminants from the top surface of substrate, ultrasonic cleaning in a bath of acetone and ethanol was used. (2) By soaking of substrate in deionized water, SrO or TiO_2 of $SrTiO_3$ surface reacts with water to form hydroxide complexes. (3) During etching with buffered oxide etchant (BOE) of NH_4F: HF = 7:1 for 50 s, the hydroxide complexes dissolves in the acidic solution. (4) The chemically treated substrate are annealed at 900 ℃ for 10 hours. Finally, we can obtain atomically flat TiO_2-terminated surfaces with step-and-terrace morphology (**Fig. S12a**). Moreover, a line profile across AFM image (**Fig. S12b**) exhibits atomic steps and terraces structures with one unit-cell step height (~0.39 nm).

Reference

1. S. Y. Yang, L. W. Martin, S. J. Byrnes, T. E. Conry, S. R. Basu, D. Paran, L. Reichertz, J. Ihlefeld, C. Adamo, A. Melville, Y. H. Chu, C. H. Yang, J. L. Musfeldt, D. G. Schlom, J. W. Ager and R. Ramesh, *Applied Physics Letters*, 2009, **95**, 062909.
2. W. Dong, Y. Guo, B. Guo, H. Liu, H. Li and H. Liu, *Materials Letters*, 2013, **91**, 359-361.
3. R. K. Katiyar, A. Kumar, G. Morell, J. F. Scott and R. S. Katiyar, *Applied Physics Letters*, 2011, 99, 092906.
4. M. Alexe and D. Hesse, *Nature Communications*, 2011, **2**, 256.
5. R. K. Katiyar, P. Misra, S. Sahoo, G. Morell and R. S. Katiyar, *Journal of Alloys and Compounds*, 2014, **609**, 168-172.
6. T. L. Qu, Y. G. Zhao, D. Xie, J. P. Shi, Q. P. Chen and T. L. Ren, *Applied Physics Letters*, 2011, **98**, 173507.
7. B. Chen, M. Li, Y. Liu, Z. Zuo, F. Zhuge, Q. F. Zhan and R. W. Li, *Nanotechnology*, 2011, **22**, 195201.
8. Y. Zang, D. Xie, X. Wu, Y. Chen, Y. Lin, M. Li, H. Tian, X. Li, Z. Li, H. Zhu, T. Ren and D. Plant, *Applied Physics Letters*, 2011, **99**, 132904.
9. S. Martin, N. Baboux, D. Albertini and B. Gautier, *Rev Sci Instrum*, 2017, **88**, 023901.
10. M. S. Dresselhaus, G. Dresselhaus, R. Saito and A. Jorio, *Physics Reports*, 2005, **409**, 47-99.
11. S. Li, S. Sakurai, D. N. Futaba and K. Hata, *Nanoscale*, 2015, **7**, 1280-1284.
12. Z. Tan, L. Hong, Z. Fan, J. Tian, L. Zhang, Y. Jiang, Z. Hou, D. Chen, M. Qin, M. Zeng, J. Gao, X. Lu, G. Zhou, X. Gao and J.-M. Liu, *NPG Asia Materials*, 2019, **11,** 20.
13. X. Cui, Y. Li, X. Li and X. Hao, *Journal of Materials Chemistry C*, 2020, **8**, 1359-1365.
14. R. Gao, C. Fu, W. Cai, G. Chen, X. Deng and X. Cao, *Journal of Electronic Materials*, 2017, **46**, 2373-2378.
15. Z. Huang, P. Li, Z. Fan, H. Fan, Q. Luo, C. Chen, D. Chen, M. Zeng, M. Qin, Z. Zhang, X. Lu, X. Gao and J.-M. Liu, *physica status solidi (RRL) - Rapid Research Letters*, 2018, **12**, 1700301.
16. Y. Zhu, K. Deng, H. Sun, B. Gu, H. Lu, F. Cao, J. Xiong and L. Li, *Adv Sci (Weinh)*, 2018, **5**, 1700614.
17. A. S. R. Bati, L. Yu, S. A. Tawfik, M. J. S. Spencer, P. E. Shaw, M. Batmunkh and J. G. Shapter, *iScience*, 2019, **14**, 100-112.
18. D. B. Khadka, Y. Shirai, M. Yanagida, J. W. Ryan and K. Miyano, *Journal of Materials Chemistry C*, 2017, **5**, 8819-8827.
19. A. A. B. Baloch, F. H. Alharbi, G. Grancini, M. I. Hossain, M. K. Nazeeruddin and N. Tabet, *The Journal of Physical Chemistry C*, 2018, **122**, 26805-26815.